remote sensing

MDPI

Article

NO_2 Retrieval from the Environmental Trace Gases Monitoring Instrument (EMI): Preliminary Results and Intercomparison with OMI and TROPOMI

Liangxiao Cheng [1,2], Jinhua Tao [1,*], Pieter Valks [3], Chao Yu [1], Song Liu [3], Yapeng Wang [1,2], Xiaozhen Xiong [4,5], Zifeng Wang [1] and Liangfu Chen [1]

1 State Key Laboratory of Remote Sensing Science, Aerospace Information Research Institute, Chinese Academy of Sciences, Beijing Normal University, Beijing 100101, China; chenglx@radi.ac.cn (L.C.); yuchao@radi.ac.cn (C.Y.); wangyp@radi.ac.cn (Y.W.); wangzf@radi.ac.cn (Z.W.); chenlf@radi.ac.cn (L.C.)
2 University of Chinese Academy of Sciences, Beijing 100049, China
3 Institut für Methodik der Fernerkundung, Deutsches Zentrum für Luft- und Raumfahrt, 82234 Oberpfaffenhofen, Germany; pieter.valks@dlr.de (P.V.); Song.Liu@dlr.de (S.L.)
4 Earth System Science Interdisciplinary Center, University of Maryland, College Park, MD 20740, USA; xiaozhen.xiong@noaa.gov
5 Science Systems and Applications Inc., 10210 Greenbelt Road, Lanham, MD 20706, USA
* Correspondence: taojh@radi.ac.cn

Received: 14 November 2019; Accepted: 9 December 2019; Published: 14 December 2019

Abstract: Onboard the Chinese GaoFen-5 (GF5) satellite, the Environmental trace gases Monitoring Instrument (EMI) is a nadir-viewing wide-field spectrometer that was launched on May 9, 2018. EMI measures the back-scattered earthshine solar radiance in the ultraviolet and visible spectral range. By using the differential optical absorption spectrometry (DOAS) method and the EMI measurements in the VIS1 band (405–465 nm), we performed retrievals of NO_2. Some first retrieval results of NO_2 from EMI and a comparison with OMI and TROPOMI products are presented in this paper. The monthly mean total vertical column densities (VCD) of NO_2 show similar spatial distributions to OMI and TROPOMI ($r > 0.88$) and their difference is less than 27%. A comparison of the daily total VCD shows that EMI could detect the NO_2 patterns in good agreement with OMI ($r = 0.93$) and TROPOMI ($r = 0.95$). However, the slant column density (SCD) uncertainty (0.79×10^{15} molec cm^{-2}) of the current EMI algorithm is relatively larger than OMI. The daily variation pattern of NO_2 from EMI in Beijing in January 2019 is consistent with TROPOMI ($r = 0.96$). The spatial distribution correlation of the tropospheric NO_2 VCD of EMI with OMI and TROPOMI is 0.88 and 0.89, respectively, but shows an overestimate compared to OMI (15%) and TROPOMI (23%), respectively. This study demonstrates the capability of using EMI for global NO_2 monitoring.

Keywords: GaoFen 5; Environmental trace gases Monitoring Instrument; DOAS; stratosphere and troposphere NO_2

1. Introduction

Nitrogen oxides ($NOx=NO+NO_2$) play a key role in both stratospheric and tropospheric chemistry. In the stratosphere, they lead to ozone destruction by direct reactions with atomic oxygen and through being in the reaction cycles of halogen compounds [1]. In the lower troposphere, NOx is a critical precursor to surface ozone [2] and the titration effect of NOx also consumes O_3 [3]. Both NOx and volatile organic compounds (VOCs) impact the ozone photochemically [4]. Secondary organic aerosol (SOA) formation from aromatic hydrocarbon photooxidation is highly sensitive to the NO concentration [5]. Nitrogen dioxide (NO_2) is more stable than NO in the atmosphere, which is primarily located in the stratosphere over remote regions. In contrast, up to 90% of the total NO_2 column may be located in the troposphere over polluted regions [6]. For instance, it has been shown that there was a continuous increasing pattern for NO_2 from 2005 to 2012 over China [7]. Thereafter, it showed a decreasing trend in China due to regulations [8–10]. Over less polluted regions, natural emissions from microbiological processes in soils, wildfires, and lightning processes also influence the ambient NOx concentration and contribute to the vertical distribution of NOx. Besides, NOx is also a precursor to secondary aerosol (nitrate) through gas-to-particle conversion [11].

Satellite observations of the vertical column density (VCD) of tropospheric NO_2 from nadir-viewing UV/VIS backscatter instruments have been widely used for air quality monitoring since the mid-1990s. The Global Ozone Monitoring Experiment (GOME) onboard the European Space Agency (ESA) [12], with a spatial resolution of 320×40 km^2, revealed the weekly cycles of tropospheric NO_2 VCDs over specific areas [13]. The Scanning Imaging Spectrometer for Atmospheric Cartography (SCIAMACHY) onboard the ENVISAT satellite had a spatial resolution of 60×30 km^2 [14], which met the needs of urban-scale air quality monitoring. The better spatial resolution of the Ozone Monitoring Instrument (OMI), i.e., 13×24 km^2 at nadir [15], made it possible to monitor the stationary anthropogenic point sources (e.g., coal-fired power plants) [16]. GOME-2 onboard the MetOp-A/B/C satellites provided NO_2 information mid-morning, with a resolution of 40×80 km^2 [17,18]. The new generation sensor, the TROpospheric Ozone Monitoring Instrument (TROPOMI), onboard Sentinel-5-Precursor, was launched on October13, 2017 [19]. With an unprecedented spatial resolution of 3.5×5.5 km^2 at band 4 and significantly improved signal to noise ratio, TROPOMI can provide more detailed information of emission sources [20]. In order to further monitor the air pollution, as well as improve the air quality on a global scale, the Environmental trace gases Monitoring Instrument (EMI), which is the main focus of this study, is located onboard the Chinese GaoFen-5 (GF5) satellite launched on 9 May, 2018 [21,22]. It is the first sensor designed in China for trace gas monitoring with a relatively higher spatial resolution (13×12 km^2) than OMI.

Tropospheric NO_2 VCD retrieval from satellites consists of three key steps: spectral fitting, stratosphere-troposphere separation (STS), and tropospheric air mass factor (AMF) calculations [23–27]. The spectral fitting step obtains the total NO_2 slant column density (SCD; the integral of target trace gas along the effective light path from the sun through the atmosphere to the instrument) from the satellite-measured radiance spectrum by means of the differential optical absorption spectrometry (DOAS) method. Then, the STS step estimates the stratospheric NO_2 concentration and removes it from the total SCD to get the tropospheric SCD. Finally, the tropospheric AMF is calculated to convert the tropospheric SCD to tropospheric VCD. In recent years, the tropospheric NO_2 retrieval algorithm has seen continuous improvements in these three aspects.

In terms of DOAS fitting, van Geffen et al. (2015) improved the spectral fitting of NO_2 from OMI in the 405–465 nm spectral window by updating the wavelength calibration, improving the OMI slit function, and accounting for the weak absorbers of the O_2–O_2 collision complex and liquid water [6]. Most OMI SCD retrieval algorithms from the QA4ECV (http://www.qa4ecv.eu/) consortium's institutes are adopting the optical depth fitting method in the spectral range of 405–465 nm and including the intensity offset correction [28]. The newly updated DOAS retrieval algorithm for the GOME-2 instrument applies linear intensity offset correction to counteract the additional contribution to the scattering intensity [29].

One of the earliest STS methods is the reference sector method (RSM), which assumes that the contribution of the troposphere in the clean Pacific region can be neglected, so the total column in this region can be regarded as the proxy of the global stratosphere NO_2 column [23]. However, this simple method can causes systematic artifacts in the stratosphere. Thereafter, a modified reference sector method (MRSM) was proposed by Bucsela et al. (2013), which defines "unpolluted" pixels based on the a priori knowledge of the tropospheric contribution derived from a global chemical transport model (CTM) [26,30]. There is another method that directly uses the stratospheric NO_2 concentrations provided by CTMs for STS. However, the results of these two methods greatly depend on the CTM output [27,31]. Recently, stratospheric NO_2 column estimation was improved by the STRatospheric Estimation Algorithm from the Mainz (STREAM) method, which is a flexible and robust algorithm and requires no auxiliary data from chemical transport models. It directly determined the stratospheric NO_2 concentration based on the total column measurements by assigning a high weighting factor for mid-altitude cloudy pixels and a low weighting factor for potentially polluted pixels. It has been successfully applied to estimate the stratospheric NO_2 from GOME, SCIAMACHY, GOME-2, and OMI instruments [32].

Tropospheric AMF is the largest uncertainty source of tropospheric NO_2 retrievals, especially for polluted regions [33]. It is calculated by a radiative transfer model (RTM) and is affected by many factors, e.g., surface pressure, surface albedo, viewing geometry, and a priori profiles. Previous studies have put forward many improvements in AMF calculation to consider these factors more realistically. For instance, Lin et al. (2014, 2015) adjusted the surface pressure information from GOES CTM by the GMTED2010 surface elevation dataset [34,35]. Besides, the higher-resolution a priori NO_2 profiles from TM5-MP CTM have been used in several studies to derive AMFs [28,29,36].

Inspired by the development of sensors and algorithms and to fulfill the EMI's potential application in air quality monitoring, in this study, a total and tropospheric NO_2 retrieval algorithm based on EMI measurements is presented, which also includes the three key steps introduced above. A brief description of the EMI instrument and data used in this study are given in Section 2. The NO_2 retrieval algorithm for EMI is presented in Section 3, and some preliminary results and comparisons with OMI and TROPOMI NO_2 products are presented in Section 4. Section 5 gives a summary and the path forward for this work.

2. Data

As part of the China high-resolution earth observation system (CHEOS) project [37], GF5 is flying in a sun-synchronous polar orbit, with an orbital altitude of 705 km and the ascending equator crossing time of 13:30 [22]. EMI has two ultraviolet bands—UV1 (240–315 nm) and UV2 (311–403 nm)—and two visible bands—VIS1 (401–550 nm) and VIS2 (545–710 nm). Each band adopts an Offner imaging spectrometer and a two-dimensional charge-coupled device (CCD) with the spectral resolution ~0.3–0.5 nm. As shown in Figure 1, the swath width of the VIS1 band is approximately 2600 km, which enables it to obtain a daily global coverage. The CCD in the VIS1 band has 111 row detectors and 1286 spectral detectors, and with the binning factor of 4, the nadir spatial resolution is 12 km (across-track direction) × 13 km (along-track direction). The designed SNR for the VIS1 band is better than 1300 [22] and enables it to meet the requirements of NO_2 retrieval.

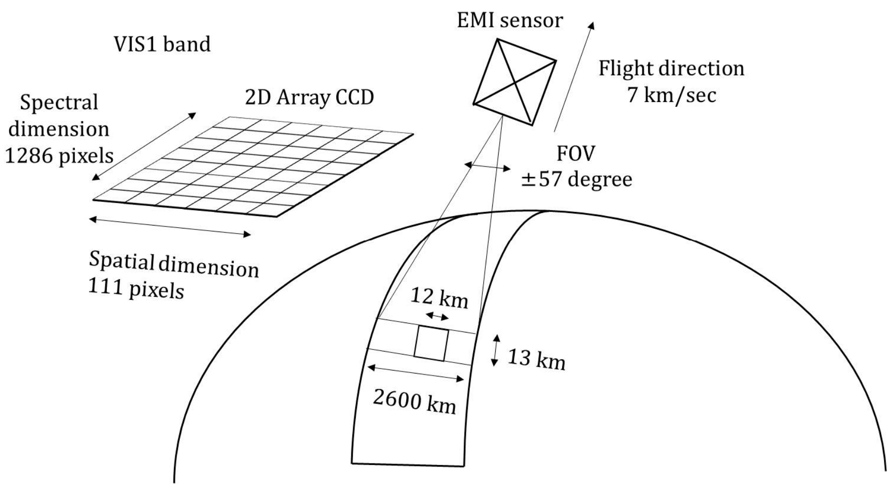

Figure 1. Environmental trace gases Monitoring Instrument (EMI) observation sketch map.

To evaluate the first EMI NO_2 results, NO_2 products from OMI and TROPOMI were used in this study for intercomparison. OMI is the Dutch-Finnish UV-Vis spectrometer aboard the EOS-Aura satellite that was launched on 15 July, 2004, with a local overpass time of 13:40 (ascending node). It has two ultraviolet bands—UV-1 (270–310 nm) and UV-2 (310–365 nm)—and one visible band (VIS, 365–500 nm). Each band is a two-dimensional CCD that simultaneously observes the direct and atmospheric backscattered sunlight for 60 individual rows [15]. With a spectral resolution of 0.63 nm and a nadir spatial resolution of 13 km × 24 km, measurements from the OMI VIS band could be used for NO_2 retrieval.

TROPOMI is a single payload developed by The Netherlands and European Space Agency (ESA) onboard the S5P satellite, which was launched on 13 October, 2017. It is flying in a sun-synchronous orbit with an ascendant overpass time of 13:30 [19]. It has four spectrometers that cover the UV–VIS–NIR–SWIR with seven bands, wherein the spectral range of the fourth band is 405–500 nm, which can be used for NO_2 monitoring. The spectral resolution and spatial resolution of band 4 are 0.55 nm and 5.5 km × 3.5 km, respectively.

With similarly designed specifications as OMI, EMI has a slightly higher spatial resolution than OMI (13 km × 24 km), and the local solar time at the ascending node (LTAN) of EMI is 10 minutes earlier than OMI (13:40). TROPOMI has a better spatial resolution (5.5 km × 3.5 km), and the LTAN (13:30) is nearly the same as EMI. Since these three instruments are similar, the OMI and TROPOMI NO_2 products are ideal data for the evaluation of EMI results.

The OMI NO_2 product used in this study is the latest version (SPv3) obtained from the NASA website (https://disc.gsfc.nasa.gov/datasets). The OMI NO_2 SCD fitting adopts the method presented by Marchenko et al. (2015), with a bias of 1.2×10^{15} molec cm^{-2} and noise of $0.9 \pm 0.3 \times 10^{15}$ molec cm^{-2}. The a priori NO_2 profiles used in the AMF calculations are from the GMI, which is a three-dimensional CTM, with 72 atmospheric vertical levels from the surface to 0.01 hPa. The stratosphere-troposphere separation (STS) adopted in the current NASA algorithm is the modified reference sector method (MRSM) proposed by Bucsela et al. (2013). This STS method determines the “unpolluted” observation pixels based on the monthly mean NO_2 profile rather than a fixed “regional mask”, which has the advantage that it reserves more observation in the continental area in cases of cloud shielding, thus reducing the interpolation error.

The TROPOMI NO_2 product (offline v.101) is available from https://s5phub.copernicus.eu/. The SCD fitting method for the TROPOMI algorithm follows Boersma et al. (2011) and Van Geffen et al. (2015), with a fitting error of about 0.5–0.6 × 10^{15} molec cm^{-2}. The a priori NO_2 profiles used in the AMF calculation are derived from the TM5-MP model, which includes the troposphere and stratosphere, separated by the tropopause index. The baseline STS method for TROPOMI includes the data assimilation of slant columns in the TM5-MP CTM, which provides an estimate of the stratospheric contribution to the NO_2 slant columns.

3. EMI NO_2 Retrieval Algorithm

3.1. Spectral Fitting

Based on the Beer–Lambert law, the DOAS method is widely used to retrieve trace gases such as O_3, NO_2, SO_2, and HCHO in the UV-VIS spectral range. The spectral fitting in this study is based on optical density fitting [38]:

$$\tau(\lambda) = -ln[\frac{I(\lambda - \Delta(\lambda)) - offset(\lambda)}{I_0(\lambda)}] = \sum_i \sigma_i'(\lambda) SCD_i + \sum_p a_p \lambda^p \quad (1)$$

where, $\tau(\lambda)$ represents the optical density, I the measured radiance, I_0 the measured irradiance, $\Delta(\lambda)$ the wavelength shift of radiance, $offset(\lambda)$ the intensity offset, $\sigma_i'(\lambda)$ the absorption cross-section (ACS), SCD_i the fitted SCD, a_p the polynomial coefficient and p the order of polynomial.

Table 1 lists the fitting parameters used in the EMI NO_2 spectral fitting, and for comparison, the corresponding settings of OMI-NASA (SPv3) and TROPOMI NO_2. The single irradiance data measured on June 12, 2018, was used as the reference spectrum during the spectral fitting. The NO_2 SCDs represent fitting in the wavelength interval of 405–465 nm using a fifth polynomial. The ACS of NO_2 [39] [220 K], O_3 [40] [223 K], H_2O vapor [41,42], H_2O liquid [43], and O_4 [44] are all degraded to the EMI spectral resolution, and then used in the fitting process. These were made by convolving the cross sections with the slit functions for different cross-track positions. Besides, the Ring effect was also taken into account by including an additional pseudo ACS, which was calculated by convolving the solar spectrum with the Raman cross sections. Intensity offset correction was also applied to the radiance spectrum. In this study, the spectral fitting step was implemented by using QDOAS software developed at the Belgian Institute for Space Aeronomy (BIRA-IASB) [45]. It should be noted that only pixels with small solar zenith angles (<80) and small cloud fractions (<0.2) were taken into consideration.

Table 1. Spectral fitting parameter settings for EMI, the Ozone Monitoring Instrument (OMI), and the TROpospheric Ozone Monitoring Instrument (TROPOMI).

Parameters		EMI	OMI-NASA [46]	TROPOMI [47]
Fitting window		405–465 nm	402–465 nm	405–465 nm
Reference spectrum I_0		Irradiance measured on 12 June, 2018	Monthly mean solar irradiance	Annual mean (2005) solar reference
Polynomial		5th-order	Two in seven microwindows: (402–410), (409–418), (415–425), (424–434), (433–444), (438–453), and (451–465)	5th-order
Included cross sections	CHOCHO	×	√ (296 K)	×
	O_3	√ (223 K)	×	√ (243 K)
	NO_2	√ (220 K)	√ (220 K)	√ (220K)
	O_4	√ (293 K)	×	√ (293 K)
	H_2O vapor	√ (280 K)	√ (280 K)	√ (280 K)
	H_2O (liquid)	√	×	√ (295 K)
	Ring Effect	√	√Air+water	√
Offset correction		√	×	×

3.1.1. Wavelength Calibration

The DOAS algorithm is very sensitive to a wavelength shift. Even a very small wavelength shift (~0.002 nm) will introduce large uncertainties into the SCD fitting results of NO_2 [46]. For EMI irradiance and radiance data, the original wavelength grid can be obtained by a third-degree polynomial:

$$\lambda(i) = a_0 + a_1 i + a_2 i^2, i = 0 \sim N - 1 \tag{2}$$

where, $\lambda(i)$ is the wavelength and i is the wavelength index from 0 to 1285 for VIS1 band. The coefficients a_0, a_1 and a_2 are different for each CCD row and can be read from the level1 data file.

The wavelength shift for the radiance spectrum is obtained by solving Equation (1). For irradiance spectrum, the wavelength calibration is achieved by using a highly accurate solar atlas as the reference [48], and minimizing the cost function, which describes the discrepancy between the measured solar spectrum and reference solar spectrum. Two parameters are defined during the calibration: the wavelength shift that represents a wavelength increment with the unit of nm and wavelength squeeze, which is a dimensionless variable representing a correction to the width of the spectral pixel. The wavelength grid can be updated by adjusting the two parameters:

$$\lambda^*(i,\alpha,\beta) = (a_0+\alpha) + (a_1 \times \beta \times i) + a_2 i^2, i = 0 \sim N-1 \quad (3)$$

where α is shift, β is squeeze. Then, the cost function can be described as the following equation:

$$\chi^2(L,\alpha,\beta) = \frac{1}{N-2}\sum_{i=1}^{N}[G^*(i) - L \otimes S^*(i,\alpha,\beta)]^2 \quad (4)$$

where L is the slit function, $G(i)$ is the measured solar spectrum, $S^*(i,\alpha,\beta)$ is the reference solar spectrum that interpolated to the updated wavelength grid. The factor $1/(N-2)$ represents the degrees of freedom and the symbol $\otimes$ represents convolution.

3.1.2. Slit Function Treatment

One of the key parameters which are related to the spectral fitting is the slit function of each detector. The slit function can not only be used to convolve with high-resolution solar spectra during the wavelength calibration procedure, but also to convolve with high-resolution absorption cross sections during the spectral fitting procedure [49]. The slit function can be fitted during the irradiance calibration procedure. Figure 2 shows the slit function of the EMI VIS1 band before and after the launch. The change of slit function is obvious, with a mean value of 13.6%. The largest change appeared on the 73rd row with a value of 31.4% and the smallest change appeared on the 23^{rd} row with a value of 0.1%. Furthermore, the viewing angle dependency is also obvious, which means that different slit functions should be used, according to the different rows.

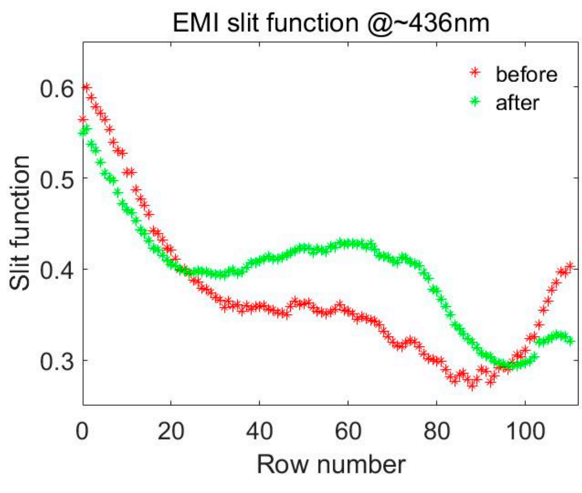

Figure 2. The slit function of the EMI VIS1 band before and after the launch.

3.1.3. De-Stripe Correction

The fitted NO_2 SCD from EMI exhibits non-physical "stripes" (Figure 3a) like OMI [26,31], which could result from the calibration error in the irradiance data [24]. These biases, which appeared in the initial SCD results, need to be removed by spatial filtering before subsequent procedures. The de-striping method used in this study is based on the method proposed by Boersma et al. (2007) for the early phase of OMI data. Some adjustments are as follows: Firstly, owing to the presence of cloud pixels, the variance for the whole window cannot be calculated. Therefore, variances of pixels in the along-track direction of each row were calculated to find a window with the least total variance. Secondly, only the first Fourier term was considered as the low frequency to be removed.

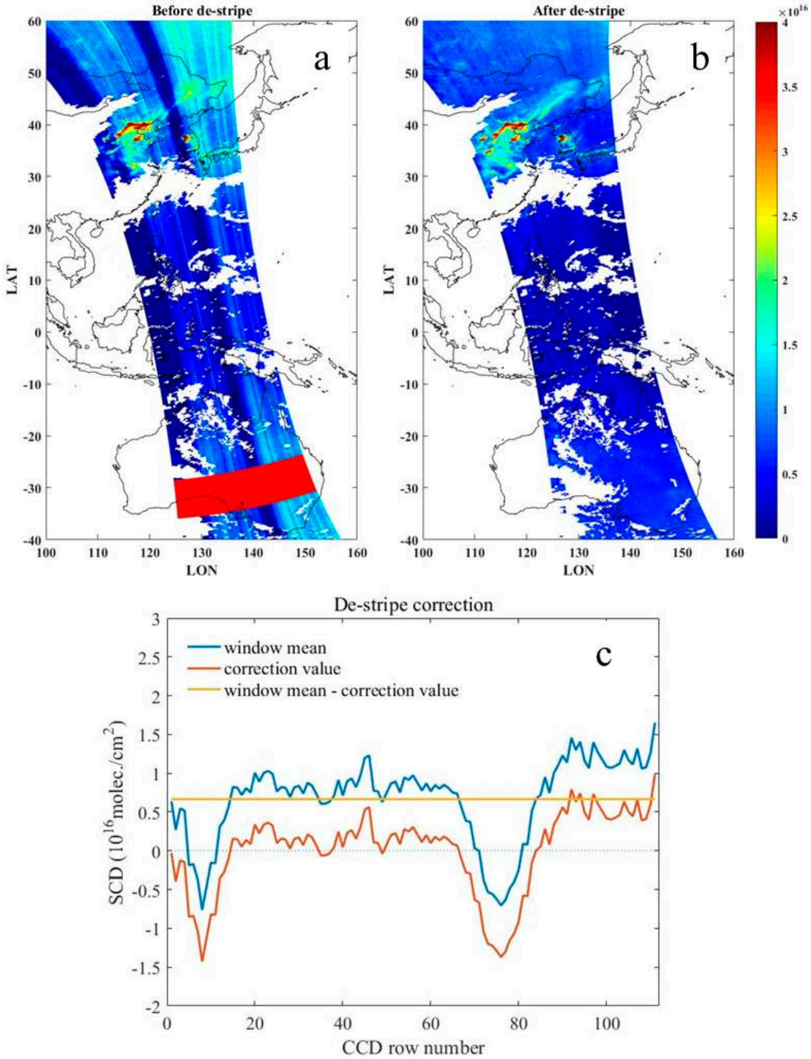

Figure 3. EMI NO_2 slant column density (SCD) (**a**) before and (**b**) after de-stripe correction (**c**). The data shown here is a swath overpass China region on November 3, 2018. Pixels with cloud cover have been removed.

Taking the data of a swath overpass China region on November 3, 2018 as an example (Figure 3), the steps of de-stripe correction are as follows:

(1) Find the potential windows with the size of 111 across-track pixels by 100 along-track pixels in the whole orbit with SZA < 80°, and then compute the total variance of the 111 rows in each potential window and pick the window with the smallest total variance (red window in Figure 3a);

(2) For the selected window, use the pixels in the along-track direction to obtain 111 values of the averaged SCD (blue line in Figure 3c);

(3) Convert the 111 mean values into the frequency domain by Fourier analysis and remove the first term with the lowest frequency, and then convert the remaining frequencies into 111 correction values (red line in Figure 3c) by an inverse Fourier transform.

The selected window of this case has the minimum variance summation of 6.35×10^{15} molec cm^{-2}, representing the minimum SCD variation in the along-track direction. The total SCD after de-stripe correction is shown in Figure 3b, and the averaged value of each row in the selected window is 5.86×10^{15} molec cm^{-2} (yellow line in Figure 3c).

3.2. Stratosphere-Troposphere Separation (STS)

The STREAM STS method directly estimates the stratospheric concentration based on the satellite measurements over remote regions and under cloudy conditions where tropospheric contribution is considered to be negligible [32], which provides a good reference for STS on EMI. The STREAM method defined three weighting factors:

(1) Pollution weight, which was calculated using the multi-year monthly averaged climatological tropospheric NO_2 column to provide lower weights for the measurements over polluted regions;

(2) Cloud weight, which was calculated based on the cloud radiation fraction and cloud pressure to provide higher weights for cloudy measurements;

(3) Tropospheric residue weight, which was calculated during the iteration process to adjust the total weight.

The total weight was obtained on the basis of the weighting factors above. Then, two convolution kernels defined for the polar and equatorial regions, respectively, were used for the weighted convolution of the initial total column with total weight on a 1° × 1° grid to get the stratospheric NO_2 field. The initial total column used in the convolution was "latitudinally corrected" by subtracting the corresponding mean column over clean regions for each latitude band.

Figure 4 show the stratospheric VCD results derived from the STREAM algorithm for OMI orbit 75,102 and EMI orbit 1629, respectively. The spatial distribution of stratospheric VCD from EMI agrees quite well with the OMI results, and the latitudinal dependencies are clearly visible in the stratospheric VCD for both OMI and EMI. The stratospheric VCD results from EMI in the mid-high northern hemisphere are a little higher than those from OMI, which could be attributed to the relatively higher total VCD in these regions. The tropospheric residue results of EMI and OMI are, overall, in the same order of magnitude, and the mean tropospheric residue over the Pacific region for EMI (OMI) is 12 (9) × 10^{13} molec cm^{-2}, which is within reasonable limits.

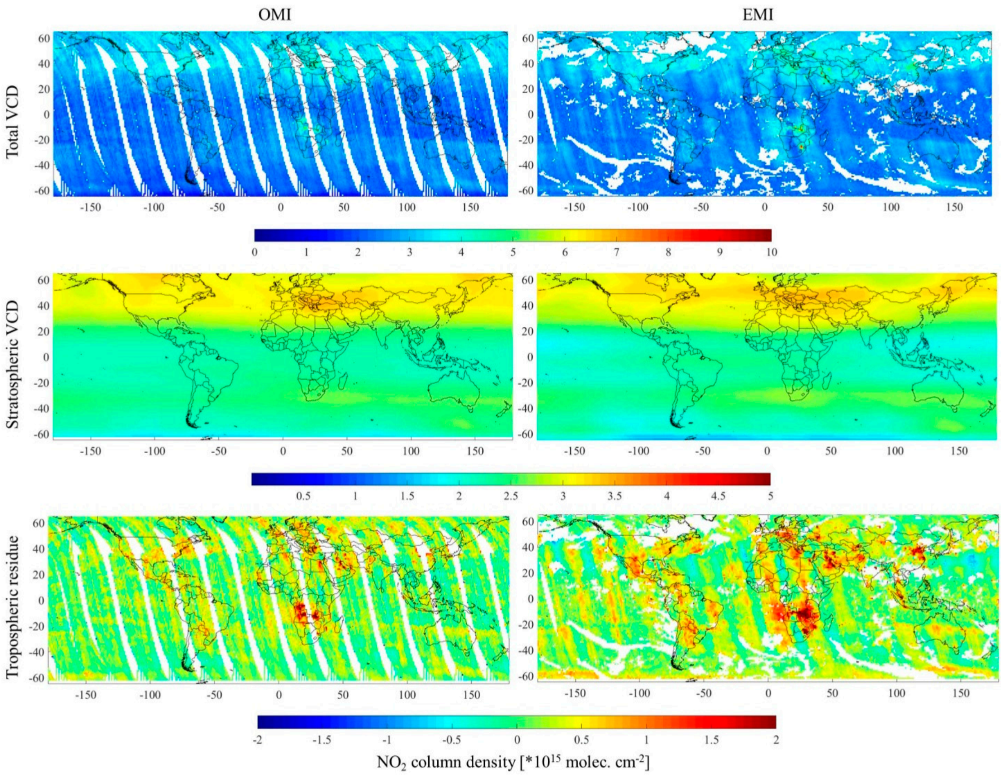

Figure 4. Total vertical column densities (VCD) (**top**), stratospheric VCD (**middle**), and tropospheric residue (**bottom**) derived from the STRatospheric Estimation Algorithm from the Mainz (STREAM) algorithm for OMI 75,102 orbit (**left**) and EMI 1629 orbit (**right**).

3.3. AMF Calculation

Tropospheric NO_2 SCD is obtained after the STS procedure. Then, we need to convert the tropospheric SCD to tropospheric VCD, which is the main output of the EMI NO_2 retrieval algorithm, by means of the tropospheric AMF. The method for tropospheric AMF (M) calculation is adopted from Boersma et al. (2004):

$$M = \frac{\sum_l m_l x_{a,l} \cdot c_l}{\sum_l x_{a,l}} \tag{5}$$

$$c_l = 1 - 0.003[T(p) - T_0] \tag{6}$$

where m_l is the scattering weight AMF (box-AMF), $x_{a,l}$ is the NO_2 sub-column in layer l, c_l is the temperature correction factor applied to correct the absorption cross section spectrum according to the effective temperature $T(p)$ at a specific layer p, and T_0 (220K) is the temperature of the NO_2 absorption cross section used in the DOAS fitting. The independent pixel approximation (IPA) allows the calculation of AMF for a partly cloudy scene as a linear combination of cloudy (M_{cl}) and clear (M_{cr}) components:

$$M = \omega M_{cl} + (1 - \omega) M_{cr} \tag{7}$$

where ω represents the effective cloud fraction, and is obtained from the TROPOMI cloud products.

With an assumption of Lambertian equivalent surface reflectance (LER) for both the ground and clouds, the AMF was determined by pre-calculated scattering weight look-up tables (LUTs) and 437.5 nm was selected as an effective wavelength for scattering weight calculation [28]. The Unified Linearized Vector Radiative Transfer Model (UNL-VRTM) was used to calculate the scattering weight in this study. It comprises the Vector-linearized discrete ordinate radiative transfer (VLIDORT [50]) for radiative transfer simulation that meets the requirements for the scattering weight calculation [51]. The LUT is created as a function of the solar zenith angle (SZA), viewing zenith angle (VZA), relative azimuth angle (RAA), surface albedo, and elevation-dependent surface pressure. The mid-latitude summer atmospheric type with 49 fixed layers was used. Table 2 lists the nodes of these parameters in the LUTs.

Table 2. Parameters that define the box-air mass factor (AMF) look-up table (LUT).

Parameter	Number of Nodes	Grid Values
SZA (°)	16	0, 10, 20, 30, 40, 45, 50, 55, 60, 65, 70, 72, 74, 76, 78, 80
VZA (°)	9	0, 10, 20, 30, 40, 50, 60, 65, 70
RAA (°)	5	0, 45, 90, 135, 175
Albedo	14	0, 0.01, 0.025, 0.05, 0.75, 0.1, 0.15, 0.2, 0.25, 0.3, 0.4, 0.6, 0.8, 1.0
Surface/Cloud pressure (hPa)	17	1063.10, 1037.90, 1013.30, 989.28, 965.83, 920.58, 876.98, 834.99, 795.01, 701.21, 616.60, 540.48, 411.05, 308.00, 226.99, 165.79, 121.11

Given the influence of cloud on trace gas retrieval, it is necessary to determine whether the pixel is affected by cloud or not before NO_2 retrieval. As the spectra range of EMI does not cover the absorption characteristics of the O_2-A band near 760 nm, the cloud retrieval algorithm based on the O_2-A channel, as used by the TROPOMI algorithm, cannot be used for EMI. Although the cloud retrieval algorithm developed for OMI, for example, OMI/Aura Cloud Pressure and Fraction Raman Scattering [52] and OMI/Aura Cloud Pressure and Fraction O_2-O_2 Absorption [53], could be adopted for EMI, such a cloud retrieval algorithm for EMI is excluded in this paper. For simplification, other external cloud parameter products, i.e., the cloud fraction, cloud pressure, and cloud radiation fraction information from TROPOMI cloud products, are used for the AMF calculation of cloudy pixels.

The a priori NO_2 profile and surface pressure used in this study for AMF calculations were obtained from TM5-MP CTM [54]. The model provides global coverage information of 34 atmospheric layers with a 1° × 1° grid resolution and 30 min temporal frequency. The model outputs include the NO_2 profile (n_l) of the volume mixing ratio, temperature profile (T_l) in the unit of K, hybrid pressure level in the unit of Pa, and the tropopause layer index (l_{tp}) is also provided to separate the stratosphere and troposphere.

For each individual pixel, the surface albedo is obtained from the climatological monthly Lambertian equivalent reflector (OMLER) data at 440 nm [55]. The surface elevation is obtained from the GMTED2010 data, which have a uniform spatial resolution of 30 arc seconds. During the AMF calculation, the scattering weight is interpolated according to the observation condition and the pressure grid of the a priori profile.

Figure 5 shows the cloud fraction and tropospheric AMF for OMI, EMI, and TROPOMI, respectively. The pattern of the tropospheric AMF spatial distribution from EMI is consistent with OMI and TROPOMI. The area averaged tropospheric AMF of EMI (Figure 5e) is 1.20, while the corresponding value of OMI (Figure 5d) and TROPOMI (Figure 5f) is 1.25 and 1.33, respectively. For cloud-free pixels, the area averaged AMF of EMI is 1.48% higher than OMI and 6.1% lower than TROPOMI. These discrepancies could mainly result from discrepancies in the a priori NO_2 profiles.

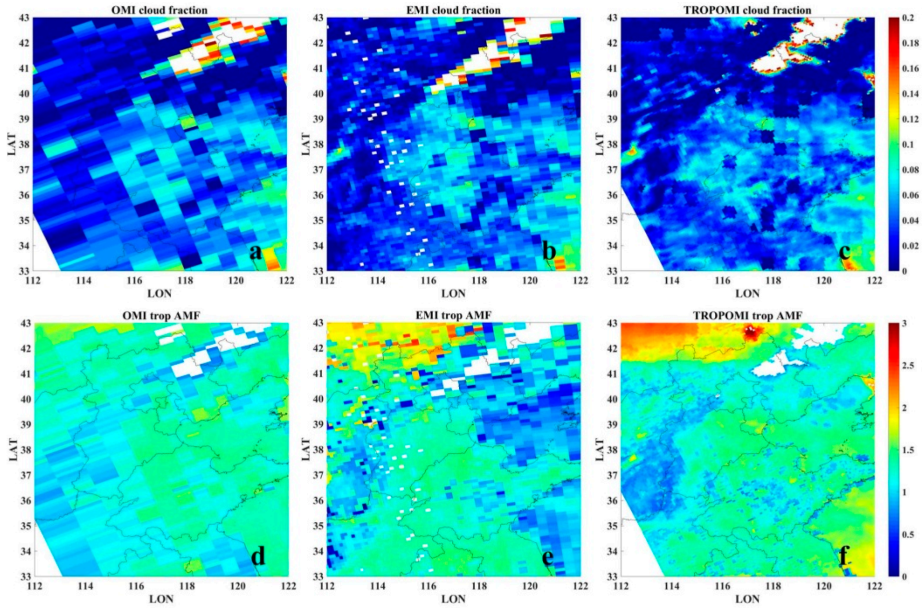

Figure 5. Cloud fractions and tropospheric AMF over the North China Plain region on 22 January, 2019 for OMI (**a**,**d**), EMI (**b**,**e**), and TROPOMI (**c**,**f**).

4. Results

4.1. Total VCD

Figure 6 displays the global monthly averaged NO_2 column density from OMI, EMI, and TROPOMI in August 2018 and January 2019, respectively. Overall, the spatial patterns are similar, particularly the low values in the tropics in January/August and high values in the northern latitudes in August, the enhanced zone in the mid-high latitudes of the northern hemisphere in August relative to January, and the huge pollution cluster in the North China Plain region in January. The spatial correlation between them is very good, with the correlation coefficient between EMI and OMI (TROPOMI) being 0.92 (0.93) in August and 0.89 (0.91) in January. However, the stripes are faintly visible in EMI, which could be due to imperfect de-striping correction. In addition, some noisy spots scattered in the ocean area are visible, which may have been caused by incomplete cloud screening.

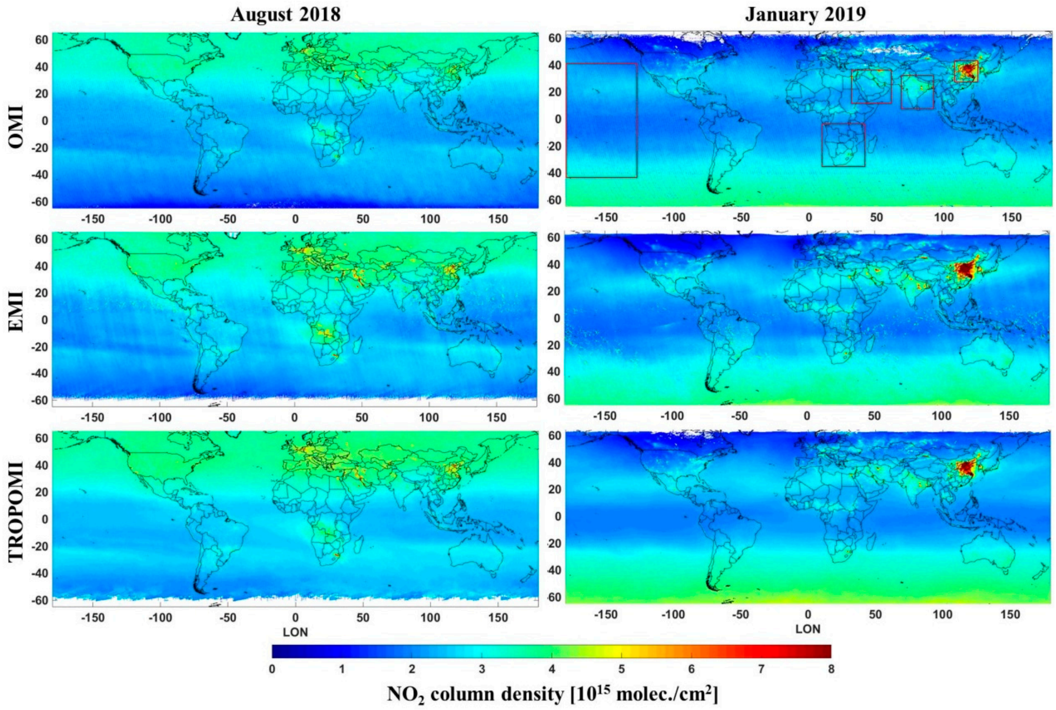

Figure 6. Monthly averaged NO_2 column density from OMI (**top** row), EMI (**middle** row), and TROPOMI (**bottom** row) in August 2018 (**left** panel) and January 2019 (**right** panel).

Overall, like OMI and TROPOMI, EMI can detect the spatial distribution of NO_2 and is capable of NO_2 pollution monitoring. A detailed comparison of EMI with OMI and TROPOMI was made by selecting five regions, i.e., Pacific, North China, South Africa, Middle East, and India, as marked in Figure 6. Figure 7 shows the statistical values of the five regions.

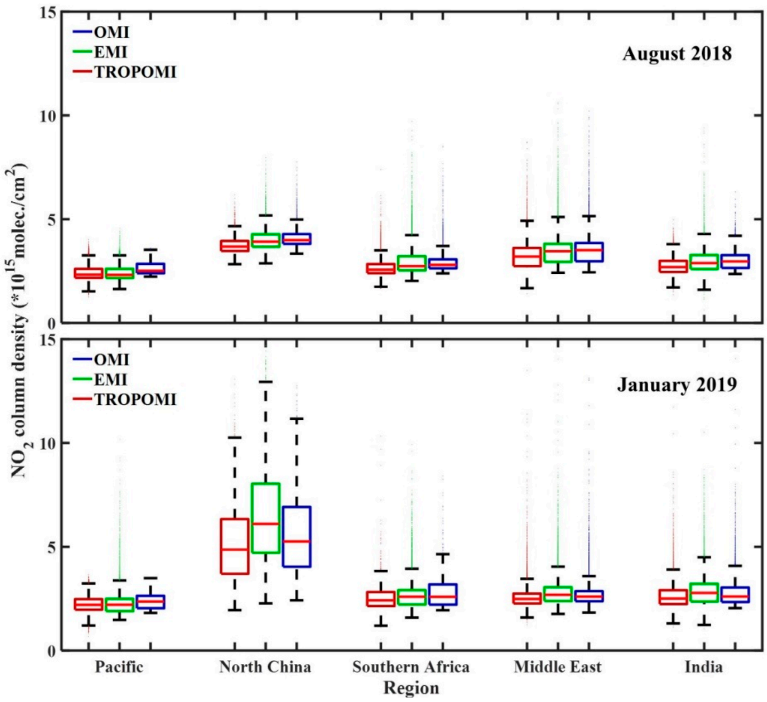

Figure 7. Regional statistics of NO_2 column density from OMI, EMI, and TROPOMI for August 2018 (**top**) and January 2019 (**bottom**).

The mean value of EMI in the Pacific region is consistent with TROPOMI in both August and January, but is lower than OMI by 10% in August and 7.5% in January, indicating that EMI can accurately reflect the background concentration in clean regions. In the other polluted regions, the mean value of EMI is, generally, higher than TROPOMI, but lower than OMI in August, and in January, EMI is higher than both OMI and TROPOMI. This is particularly evident in the North China region in January. On average, the discrepancies between EMI and OMI are within 10.5% (27.3%) in August (January), with the corresponding value between EMI and TROPOMI being 9.3% (17.2%).

Figure 8 shows a map of the NO_2 total VCD over the North China Plain region from EMI, OMI, and TROPOMI, respectively, using data from 22 January, 2019. The selection of this date is due to the severe NO_2 pollution on this day, and it is clear, so there are few pixels contaminated by cloud and few OMI pixels affected by "row anomaly". The EMI results (Figure 8a) are consistent with OMI (Figure 8b) and TROPOMI (Figure 8c) in terms of the spatial distribution, particularly over regions where high values of NO_2 are clearly visible in the EMI results. EMI gives finer NO_2 column information over polluted regions than OMI due to its relatively higher spatial resolution, e.g., the hot-spots in northern areas of Shanxi province (113°E, 37–40°N). Generally, as a supplement of OMI who has passed its designed mission lifetime, EMI can provide better spatial coverage than OMI, and, as a new sensor, it plays an important role in NO_2 monitoring.

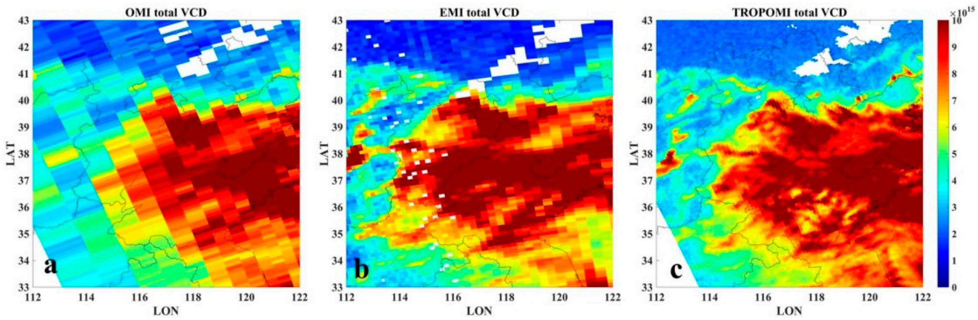

Figure 8. NO_2 total VCD results of OMI (**a**), EMI (**b**), and TROPOMI (**c**) over the North China Plain region on 22 January, 2019.

In order to further examine the consistency in spatial distribution, this region was divided into 100 boxes with a 1° × 1° size. The mean values in each box are compared in Figure 9. As expected, there is a good correlation between them, with a correlation coefficient of 0.93 (0.95) between EMI and OMI (TROPOMI). The regional averaged total VCD values of OMI and TROPOMI are 6.34×10^{15} and 6.59×10^{15} molec cm^{-2}, respectively. The corresponding value of EMI is 24.5% (19.9%) higher than OMI (TROPOMI), and these discrepancies can be attributed to the different SCD fitting parameters (Table 1), as well as the de-stripe method, used in this study.

In order to evaluate the uncertainty in the retrieved SCD, we divided the Pacific clean region (60°S–60°N; 160°E–180°E) into 2° × 2° boxes. Theoretically, the AMF of pixels within a box has little variability, and the VCD of the pixels within a box should have little difference, so the variability in the retrieved total VCD results from the error of SCD. The uncertainty of SCD can be estimated by statistically analyzing the SCD deviation between each valid EMI pixel in a box and the box mean [27]. Figure 10 shows the histograms of the absolute differences of all valid pixels in August 2018. The distribution of SCD deviation basically follows a Gaussian distribution, which demonstrated that the variability within boxes is random error. The corresponding width of the Gaussian distribution is 0.79×10^{15} molec cm^{-2}, which was interpreted as the SCD error of all valid pixels in August 2018.

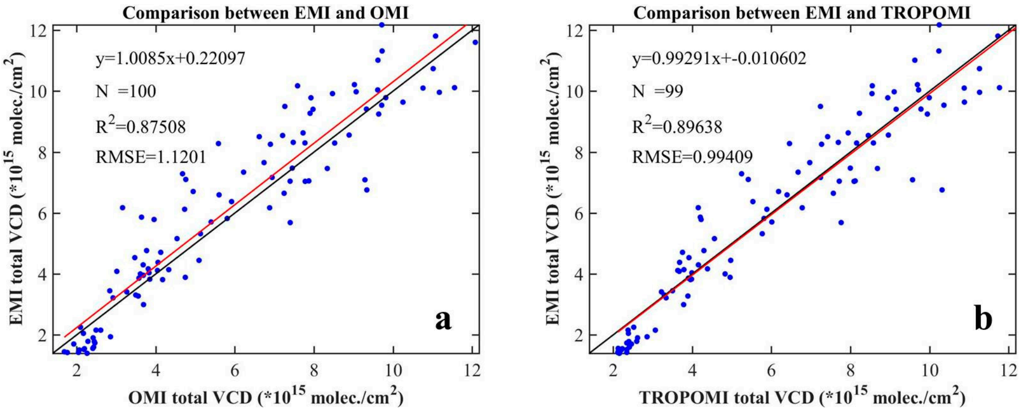

Figure 9. Total VCD comparisons between EMI and (**a**) OMI and (**b**) TROPOMI over the North China Plain region on 22 January, 2019.

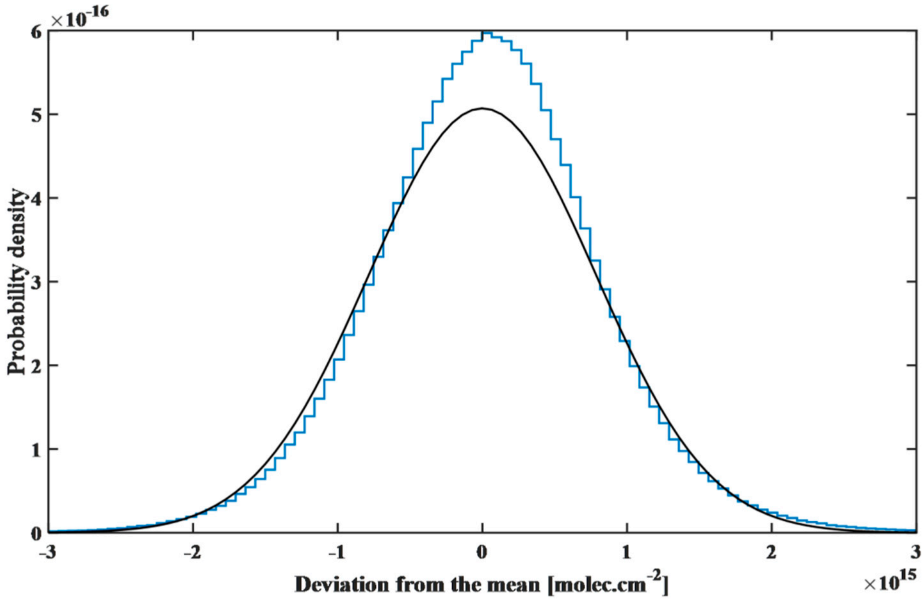

Figure 10. Distribution of the SCD deviations from box means for all valid pixels in August 2018. The black line shows a Gaussian function fitted to the histogram data. The width of the Gaussian (σ) corresponds to a slant column error of 0.79×10^{15} molec cm^{-2}.

The SCD uncertainty of the current EMI NO_2 algorithm is 17.9% larger than that of OMI (the near real-time algorithm) after its launch of more than two years [24], and also higher than the OMI algorithms presented by Zara et al. (2018). The relatively large SCD uncertainty may mainly result from the residual cloud pixels caused by the rough cloud screen method.

4.2. Tropospheric VCD

Figure 11 shows the tropospheric NO_2 VCD of OMI, EMI, and TROPOMI, respectively. On average, the tropospheric VCD of EMI (1.32×10^{16} molec cm^{-2}) is 15% and 23% higher than that of OMI (1.14×10^{16} molec cm^{-2}) and TROPOMI (1.07×10^{16} molec cm^{-2}), respectively. These discrepancies could mainly result from the tropospheric AMF. The spatial distribution of EMI is in good agreement with OMI (r = 0.88) and TROPOMI (r = 0.89), which can be seen from the scatter plot of VCD from EMI vs. OMI and TROPOMI in the bottom panel of Figure 11.

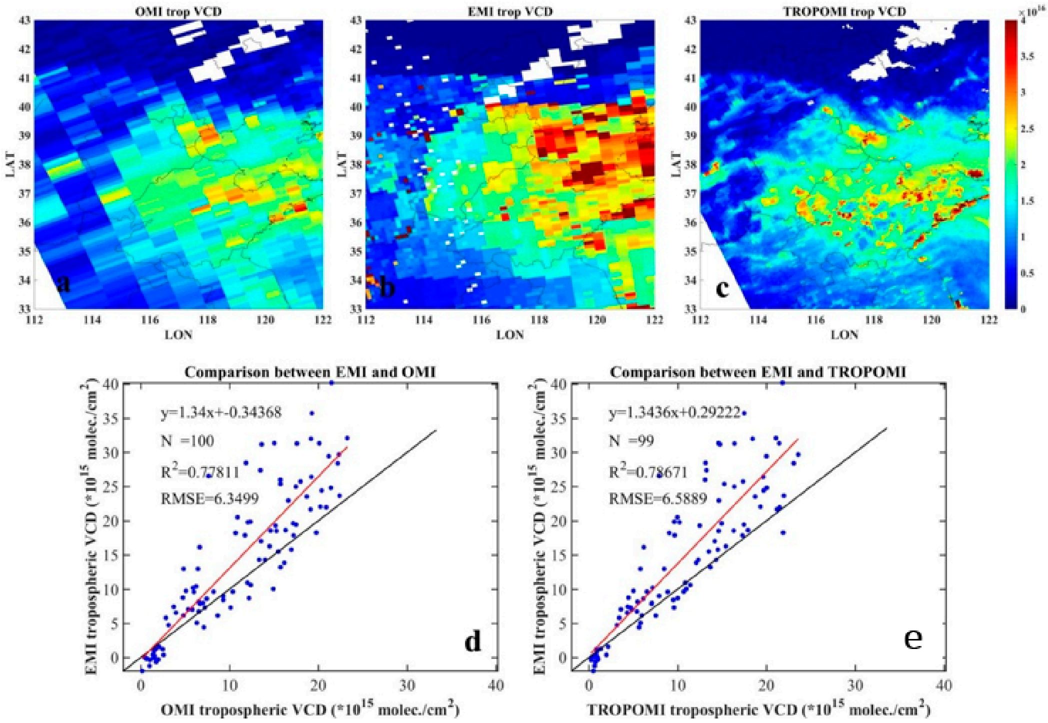

Figure 11. Tropospheric NO_2 VCD results of (**a**) OMI, (**b**) EMI, and (**c**) TROPOMI (top panel) and comparisons of EMI and OMI (**d**) and TROPOMI (**e**) over the North China Plain region on 22 January, 2019.

4.3. Application Case

Furthermore, a comparison of NO_2 VCD from EMI and TROPOMI was made by processing roughly one month data over the Beijing area. Figure 12 shows the daily variation of the mean NO_2 VCD in Beijing in January 2019. OMI data is not included in this comparison due to the serious influence of "row anomaly". There are four NO_2 pollution events in January that were caught by both EMI and TROPOMI with a correlation coefficient of 0.96, as shown in the shaded areas. Overall, the variation of EMI NO_2 VCD is larger than TROPOMI, and on the heavily polluted days, EMI NO_2 VCD is mostly higher than TROPOMI, and the largest discrepancy is up to 3.27×10^{15} molec cm^{-2} on 14 January. On the contrary, EMI NO_2 VCD is lower than TROPOMI on days with little NO_2 pollution, and the smallest discrepancy is 8×10^{12} molec cm^{-2} on 15 January. The difference between EMI NO_2 VCD and TROPOMI ranges from 0.2% to 44%.

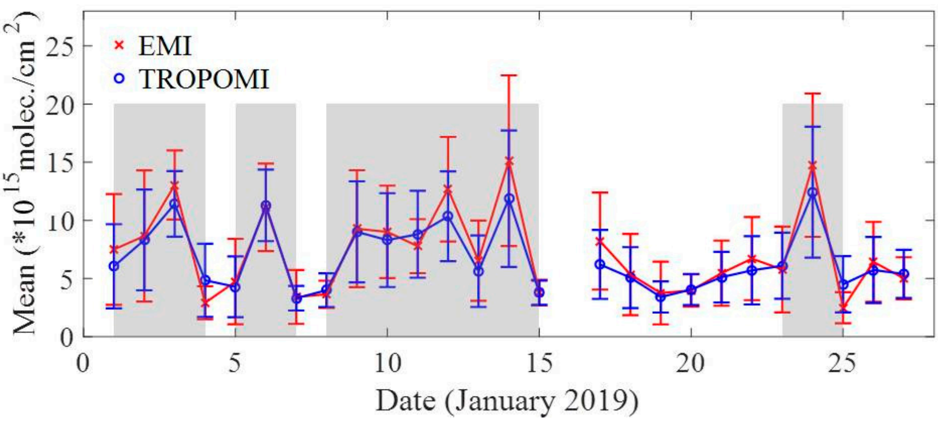

Figure 12. Daily variation of the mean NO2 VCD of EMI and TROPOMI in the Beijing area (115.5~117.5 E; 39~41 N) in January 2019.

5. Summary and Conclusions

EMI onboard the GF5 satellite was designed for trace gas monitoring in the troposphere and stratosphere. The measured earth radiance and solar irradiance in the spectral range of 401–550 nm (VIS1 band) were used for NO_2 retrieval in this study. The EMI NO_2 retrieval algorithm, as well as some results and their comparison with OMI and TROPOMI, were presented in this paper.

The comparison of the global distribution of the monthly averaged NO_2 column density shows that OMI, EMI, and TROPOMI agree with each other with $r > 0.88$; however, the discrepancy of the regional average between EMI and OMI (and TROPOMI) is within 27.3%. Using one day data over the North China Plain on 22 January, 2019, the correlation coefficient between EMI and OMI (TROPOMI) is 0.93 (0.95), but the region's averaged value of EMI is 24.5% and 19.9% higher than that of OMI and TROPOMI, respectively. The SCD uncertainty of EMI is about 0.79×10^{15} molec cm^{-2}. The spatial distribution of tropospheric AMF and VCD of EMI also agree well with OMI and TROPOMI. The comparison of the daily variation using one month data also shows a very good agreement between EMI and TROPOMI in Beijing ($r = 0.96$). The good agreement of EMI products with OMI and TROPOMI makes us confident that EMI can be used to retrieve tropospheric NO_2 and provide the daily NO_2 global distribution.

It should be noted that the results presented in this study are preliminary, and many more works related to the EMI NO_2 retrieval algorithm require further study to improve the result. For example, the cloud information is currently obtained from TROPOMI cloud products; however, due to the difference in the satellite pass time and spatial resolution, the external cloud information cannot meet the requirements of near real-time NO_2 retrieval. Cloud parameters with a sufficient precision and consistency need to be updated in the future. In addition, because of the insufficient solar irradiance measurements, the reference spectra used in this study are individual measurements from June 12, 2018. The SCD uncertainty caused by the use of single irradiance needs to be further analyzed. It is expected that, at least, weekly-to-monthly averaged reference spectra should be used in the future to reduce the retrieval uncertainty. Besides, there is an urgent need for more irradiance data, not only for trace gas retrieval, but also for the monitoring of EMI degradation. In spite of the existing shortcomings, this study may serve as a reference for the design of subsequent satellite payloads, i.e., EMI-02 and EMI-03.

Author Contributions: Conceptualization, J.T. and Liangfu Chen (L.C.); formal analysis, Liangxiao Cheng (L.C.); methodology, P.V. and S.L.; resources, Z.W.; validation, C.Y.; writing—original draft preparation, Liangxiao Cheng (L.C.) and Y.W.; writing—review and editing, X.X. and Liangxiao Cheng (L.C.).

Funding: This research was funded by the Strategic Priority Research Program of the Chinese Academy of Sciences (Grant No. XDA19040201) and the National Key Research and Development Program of China (Grant No. 2017YFB0503901).

Acknowledgments: We would like to thank the following agencies for providing the satellite data: The EMI level 1 data is provided by the Ministry of Ecology and Environment Satellite Application Center for Ecology and Environment (SACEE). The OMI OMNO2 product is archived and distributed by the Goddard Earth Sciences Data & Information Services center (NASA). The Sentinel 5 Precursor TROPOMI Level 2 NO_2 product is developed by KNMI with funding from the Netherlands Space Office (NSO) and processed with funding from the European Space Agency (ESA). We are thankful to Chunyan Zhou (SACEE, China) for the provision of EMI level 1 products, Steffen Beirle (Max Planck Institute for Chemistry) for help with the STREAM algorithm, Xiaoguang Xu (University of Nebraska, USA) for help with the use of UNL-VRTM RTM, Haijin Zhou (Anhui Institute of Optics and Fine Mechanics, China) for help with the use of EMI level 1 products, Diego Loyola (DLR, Germany) for feedback on this manuscript, Caroline Fayt for help on QDOAS software and Ronald Johannes van der A (KNMI, Netherlands) for advice on the SCD de-stripe correction. OMI data are available at https://aura.gesdisc.eosdis.nasa.gov/data/Aura_OMI_Level2/OMNO2.003/. TROPOMI data can be downloaded from https://s5phub.copernicus.eu. The GMTED2010 data can be downloaded from http://topotools.cr.usgs.gov/GMTED_viewer/.

Conflicts of Interest: The authors declare no conflicts of interest.

References

1. Solomon, S. Stratospheric ozone depletion: A review of concepts and history. *Rev. Geophys.* **1999**, *37*, 275–316. [CrossRef]
2. Duncan, B.N.; Yoshida, Y.; Olson, J.R.; Sillman, S.; Martin, R.V.; Lamsal, L.; Hu, Y.; Pickering, K.E.; Retscher, C.; Allen, D.J. Application of omi observations to a space-based indicator of no x and VOC controls on surface ozone formation. *Atmos. Environ.* **2010**, *44*, 2213–2223. [CrossRef]
3. Lei, H.; Wang, J.X.L. Sensitivities of nox transformation and the effects on surface ozone and nitrate. *Atmos. Chem. Phys.* **2014**, *14*, 1385–1396. [CrossRef]
4. Seinfeld, J.H.; Pandis, S.N. *Atmospheric Chemistry and Physics: From Air Pollution to Climate Change*; Wiley: Hoboken, NJ, USA, 2016.
5. Li, L.J.; Tang, P.; Cocker, D.R. Instantaneous nitric oxide effect on secondary organic aerosol formation from m-xylene photooxidation. *Atmos. Environ.* **2015**, *119*, 144–155. [CrossRef]
6. Van Geffen, J.H.G.M.; Boersma, K.F.; Van Roozendael, M.; Hendrick, F.; Mahieu, E.; De Smedt, I.; Sneep, M.; Veefkind, J.P. Improved spectral fitting of nitrogen dioxide from omi in the 405–465 nm window. *Atmos. Meas. Tech.* **2015**, *8*, 1685–1699. [CrossRef]
7. Richter, A.; Burrows, J.P.; Nuss, H.; Granier, C.; Niemeier, U. Increase in tropospheric nitrogen dioxide over China observed from space. *Nature* **2005**, *437*, 129–132. [CrossRef]
8. Zhang, L.; Lee, C.S.; Zhang, R.; Chen, L. Spatial and temporal evaluation of long term trend (2005–2014) of omi retrieved no 2 and so 2 concentrations in henan province, china. *Atmos. Environ.* **2017**, *154*, 151–166. [CrossRef]
9. Souri, A.H.; Choi, Y.; Jeon, W.; Woo, J.H.; Zhang, Q.; Kurokawa, J. Remote sensing evidence of decadal changes in major tropospheric ozone precursors over east asia. *J. Geophys. Res. Atmos.* **2017**, *122*, 2474–2492. [CrossRef]
10. Georgoulias, A.K.; van der A, R.J.; Stammes, P.; Boersma, K.F.; Eskes, H.J. Trends and trend reversal detection in 2 decades of tropospheric no2 satellite observations. *Atmos. Chem. Phys.* **2019**, *19*, 6269–6294. [CrossRef]
11. Si, Y.D.; Li, S.S.; Chen, L.F.; Yu, C.; Wang, H.M.; Wang, Y.P. Impact of precursor gases and meteorological variables on satellite-estimated near-surface sulfate and nitrate concentrations over the north china plain. *Atmos. Environ.* **2019**, *199*, 345–356. [CrossRef]
12. Burrows, J.P.; Weber, M.; Buchwitz, M.; Rozanov, V.; Ladstatter-Weissenmayer, A.; Richter, A.; DeBeek, R.; Hoogen, R.; Bramstedt, K.; Eichmann, K.U.; et al. The global ozone monitoring experiment (gome): Mission concept and first scientific results. *J. Atmos. Sci.* **1999**, *56*, 151–175. [CrossRef]
13. Beirle, S.; Platt, U.; Wenig, M.; Wagner, T. Weekly cycle of no2 by gome measurements: A signature of anthropogenic sources. *Atmos. Chem. Phys.* **2003**, *3*, 2225–2232. [CrossRef]
14. Bovensmann, H.; Burrows, J.P.; Buchwitz, M.; Frerick, J.; Noel, S.; Rozanov, V.V.; Chance, K.V.; Goede, A.P.H. Sciamachy: Mission objectives and measurement modes. *J. Atmos. Sci.* **1999**, *56*, 127–150. [CrossRef]
15. Levelt, P.F.; Van den Oord, G.H.J.; Dobber, M.R.; Malkki, A.; Visser, H.; de Vries, J.; Stammes, P.; Lundell, J.O.V.; Saari, H. The ozone monitoring instrument. *IEEE Trans. Geosci. Remote* **2006**, *44*, 1093–1101. [CrossRef]
16. Fioletov, V.E.; McLinden, C.A.; Krotkov, N.; Moran, M.D.; Yang, K. Estimation of SO_2 emissions using omi retrievals. *Geophys. Res. Lett.* **2011**, *38*. [CrossRef]
17. Callies, J.; Corpaccioli, E.; Eisinger, M.; Hahne, A.; Lefebvre, A. Gome-2-Metop's second-generation sensor for operational ozone monitoring. *ESA Bull. Eur. Space* **2000**, *102*, 28–36.
18. Munro, R.; Lang, R.; Klaes, D.; Poli, G.; Retscher, C.; Lindstrot, R.; Huckle, R.; Lacan, A.; Grzegorski, M.; Holdak, A.; et al. The gome-2 instrument on the metop series of satellites: Instrument design, calibration, and level 1 data processing—An overview. *Atmos. Meas. Tech.* **2016**, *9*, 1279–1301. [CrossRef]
19. Veefkind, J.P.; Aben, I.; McMullan, K.; Forster, H.; de Vries, J.; Otter, G.; Claas, J.; Eskes, H.J.; de Haan, J.F.; Kleipool, Q.; et al. Tropomi on the esa sentinel-5 precursor: A gmes mission for global observations of the atmospheric composition for climate, air quality and ozone layer applications. *Remote Sens. Environ.* **2012**, *120*, 70–83. [CrossRef]
20. Griffin, D.; Zhao, X.; McLinden, C.A.; Boersma, F.; Bourassa, A.; Dammers, E.; Degenstein, D.; Eskes, H.; Fehr, L.; Fioletov, V.; et al. High-resolution mapping of nitrogen dioxide with tropomi: First results and validation over the canadian oil sands. *Geophys. Res. Lett.* **2019**, *46*, 1049–1060. [CrossRef]

21. Zhang, C.X.; Liu, C.; Wang, Y.; Si, F.Q.; Zhou, H.J.; Zhao, M.J.; Su, W.J.; Zhang, W.Q.; Chan, K.L.; Liu, X.; et al. Preflight evaluation of the performance of the chinese environmental trace gas monitoring instrument (EMI) by spectral analyses of nitrogen dioxide. *IEEE Trans. Geosci. Remote* **2018**, *56*, 3323–3332. [CrossRef]
22. Zhao, M.J.; Si, F.Q.; Zhou, H.J.; Wang, S.M.; Jiang, Y.; Liu, W.Q. Preflight calibration of the chinese environmental trace gases monitoring instrument (EMI). *Atmos Meas Tech* **2018**, *11*, 5403–5419. [CrossRef]
23. Martin, R.V.; Chance, K.; Jacob, D.J.; Kurosu, T.P.; Spurr, R.J.D.; Bucsela, E.; Gleason, J.F.; Palmer, P.I.; Bey, I.; Fiore, A.M.; et al. An improved retrieval of tropospheric nitrogen dioxide from gome. *J. Geophys. Res. Atmos.* **2002**, *107*. [CrossRef]
24. Boersma, K.F.; Eskes, H.J.; Veefkind, J.P.; Brinksma, E.J.; van der A, R.J.; Sneep, M.; van den Oord, G.H.J.; Levelt, P.F.; Stammes, P.; Gleason, J.F.; et al. Near-real time retrieval of tropospheric no2 from omi. *Atmos. Chem. Phys.* **2007**, *7*, 2103–2118. [CrossRef]
25. Beirle, S.; Kuehl, S.; Pukite, J.; Wagner, T. Retrieval of tropospheric column densities of NO_2 from combined sciamachy nadir/limb measurements. *Atmos. Meas. Tech.* **2010**, *3*, 283–299. [CrossRef]
26. Boersma, K.F.; Eskes, H.J.; Dirksen, R.J.; van der A, R.J.; Veefkind, J.P.; Stammes, P.; Huijnen, V.; Kleipool, Q.L.; Sneep, M.; Claas, J.; et al. An improved tropospheric no2 column retrieval algorithm for the ozone monitoring instrument. *Atmos. Meas. Tech.* **2011**, *4*, 1905–1928. [CrossRef]
27. Valks, P.; Pinardi, G.; Richter, A.; Lambert, J.C.; Hao, N.; Loyola, D.; Van Roozendael, M.; Emmadi, S. Operational total and tropospheric no2 column retrieval for gome-2. *Atmos. Meas. Tech.* **2011**, *4*, 1491–1514. [CrossRef]
28. Boersma, K.F.; Eskes, H.J.; Richter, A.; De Smedt, I.; Lorente, A.; Beirle, S.; van Geffen, J.H.G.M.; Zara, M.; Peters, E.; Van Roozendael, M.; et al. Improving algorithms and uncertainty estimates for satellite no2 retrievals: Results from the quality assurance for the essential climate variables (QA4ECV) project. *Atmos. Meas. Tech.* **2018**, *11*, 6651–6678. [CrossRef]
29. Liu, S.; Valks, P.; Pinardi, G.; De Smedt, I.; Yu, H.; Beirle, S.; Richter, A. An improved total and tropospheric no2 column retrieval for gome-2. *Atmos. Meas. Tech.* **2019**, *12*, 1029–1057. [CrossRef]
30. Dirksen, R.J.; Boersma, K.F.; Eskes, H.J.; Ionov, D.V.; Bucsela, E.J.; Levelt, P.F.; Kelder, H.M. Evaluation of stratospheric no2 retrieved from the ozone monitoring instrument: Intercomparison, diurnal cycle, and trending. *J. Geophys. Res. Atmos.* **2011**, *116*. [CrossRef]
31. Bucsela, E.J.; Krotkov, N.A.; Celarier, E.A.; Lamsal, L.N.; Swartz, W.H.; Bhartia, P.K.; Boersma, K.F.; Veefkind, J.P.; Gleason, J.F.; Pickering, K.E. A new stratospheric and tropospheric NO2 retrieval algorithm for nadir-viewing satellite instruments: Applications to omi. *Atmos. Meas. Tech.* **2013**, *6*, 2607–2626. [CrossRef]
32. Beirle, S.; Hoermann, C.; Joeckel, P.; Liu, S.; de Vries, M.P.; Pozzer, A.; Sihler, H.; Valks, P.; Wagner, T. The stratospheric estimation algorithm from mainz (stream): Estimating stratospheric no2 from nadir-viewing satellites by weighted convolution. *Atmos. Meas. Tech.* **2016**, *9*, 2753–2779. [CrossRef]
33. Boersma, K.F.; Eskes, H.J.; Brinksma, E.J. Error analysis for tropospheric no2 retrieval from space. *J. Geophys. Res. Atmos.* **2004**, *109*. [CrossRef]
34. Lin, J.T.; Martin, R.V.; Boersma, K.F.; Sneep, M.; Stammes, P.; Spurr, R.; Wang, P.; Van Roozendael, M.; Clemer, K.; Irie, H. Retrieving tropospheric nitrogen dioxide from the ozone monitoring instrument: Effects of aerosols, surface reflectance anisotropy, and vertical profile of nitrogen dioxide. *Atmos. Chem. Phys.* **2014**, *14*, 1441–1461. [CrossRef]
35. Lin, J.T.; Liu, M.Y.; Xin, J.Y.; Boersma, K.F.; Spurr, R.; Martin, R.; Zhang, Q. Influence of aerosols and surface reflectance on satellite no2 retrieval: Seasonal and spatial characteristics and implications for NOx emission constraints. *Atmos. Chem. Phys.* **2015**, *15*, 11217–11241. [CrossRef]
36. Lorente, A.; Boersma, K.F.; Yu, H.; Dorner, S.; Hilboll, A.; Richter, A.; Liu, M.Y.; Lamsal, L.N.; Barkley, M.; De Smedt, I.; et al. Structural uncertainty in air mass factor calculation for NO_2 and hcho satellite retrievals. *Atmos. Meas. Tech.* **2017**, *10*, 759–782. [CrossRef]
37. Tong, X.D.; Zhao, W.B.; Xing, J.; Fu, W. Status and development of china high-resolution earth observation system and application. In Proceedings of the 2016 IEEE International Geoscience and Remote Sensing Symposium, Beijing, China, 10–15 July 2016; pp. 3738–3741.
38. Platt, U.; Stutz, J. *Differential Optical Absorption Spectroscopy: Principles and Applications*; Springer: Berlin/Heidelberg, Germany, 2008.

39. Vandaele, A.C.; Hermans, C.; Simon, P.C.; Carleer, M.; Colin, R.; Fally, S.; Merienne, M.-F.; Jenouvrier, A.; Coquart, B. Measurements of the NO2 absorption cross-section from 42,000 cm–1 to 10,000 cm–1 (238–1000 nm) at 220 K and 294 K. *J. Quant. Spectrosc. Radiat. Transf.* **1998**, *59*, 171–184. [CrossRef]
40. Malicet, J.; Daumont, D.; Charbonnier, J.; Parisse, C.; Chakir, A.; Brion, J. Ozone uv spectroscopy. Ii. Absorption cross-sections and temperature dependence. *J. Atmos. Chem.* **1995**, *21*, 263–273. [CrossRef]
41. Gordon, I.E.; Rothman, L.S.; Hill, C.; Kochanov, R.V.; Tan, Y.; Bernath, P.F.; Birk, M.; Boudon, V.; Campargue, A.; Chance, K.V.; et al. The hitran2016 molecular spectroscopic database. *J. Quant. Spectrosc. Radiat. Transf.* **2017**, *203*, 3–69. [CrossRef]
42. Rothman, L.S.; Gordon, I.E.; Babikov, Y.; Barbe, A.; Benner, D.C.; Bernath, P.F.; Birk, M.; Bizzocchi, L.; Boudon, V.; Brown, L.R.; et al. The HITRAN2012 molecular spectroscopic database. *J. Quant. Spectrosc. Radiat. Transf.* **2013**, *130*, 4–50. [CrossRef]
43. Pope, R.M.; Fry, E.S. Absorption spectrum (380–700 nm) of pure water. II. Integrating cavity measurements. *Appl. Optics* **1997**, *36*, 8710–8723. [CrossRef]
44. Thalman, R.; Volkamer, R. Temperature dependent absorption cross-sections of O 2–O 2 collision pairs between 340 and 630 nm and at atmospherically relevant pressure. *Phys. Chem. Chem. Phys.* **2013**, *15*, 15371–15381. [CrossRef] [PubMed]
45. Danckaert, T.; Fayt, C.; Van Roozendael, M.; De Smedt, I.; Letocart, V.; Merlaud, A.; Pinardi, G. *QDOAS Software User Manual Version 3.2*; Royal Belgian Institute for Space Aeronomy: Brussels, Belgium, 2019.
46. Marchenko, S.; Krotkov, N.A.; Lamsal, L.N.; Celarier, E.A.; Swartz, W.H.; Bucsela, E.J. Revising the slant column density retrieval of nitrogen dioxide observed by the ozone monitoring instrument. *J. Geophys. Res. Atmos.* **2015**, *120*, 5670–5692. [CrossRef] [PubMed]
47. van Geffen, J.H.G.M.; Eskes, H.J.; Boersma, K.F.; Maasakkers, J.D.; Veefkind, J.P. *TROPOMI ATBD of the Total and Tropospheric NO2 Data Products (Issue 1.2.0)*; s5P-KNMI-L2-0005-RP; Royal Netherlands Meteorological Institute (KNMI): De Bilt, The Netherlands, 2018.
48. Chance, K.; Kurucz, R. An improved high-resolution solar reference spectrum for earth's atmosphere measurements in the ultraviolet, visible, and near infrared. *J. Quant. Spectrosc. Radiat. Transf.* **2010**, *111*, 1289–1295. [CrossRef]
49. Beirle, S.; Lampel, J.; Lerot, C.; Sihler, H.; Wagner, T. Parameterizing the instrumental spectral response function and its changes by a super-gaussian and its derivatives. *Atmos. Meas. Tech.* **2017**, *10*, 581–598. [CrossRef]
50. Spurr, R.; Christi, M. On the generation of atmospheric property jacobians from the (v)lidort linearized radiative transfer models. *J. Quant. Spectrosc. Radiat. Transf.* **2014**, *142*, 109–115. [CrossRef]
51. Wang, J.; Xu, X.G.; Ding, S.G.; Zeng, J.; Spurr, R.; Liu, X.; Chance, K.; Mishchenko, M. A numerical testbed for remote sensing of aerosols, and its demonstration for evaluating retrieval synergy from a geostationary satellite constellation of geo-cape and goes-r. *J. Quant. Spectrosc. Radiat. Transf.* **2014**, *146*, 510–528. [CrossRef]
52. Joiner, J.; Vasilkov, A.P. First results from the omi rotational raman scattering cloud pressure algorithm. *IEEE Trans. Geosci. Remote* **2006**, *44*, 1272–1282. [CrossRef]
53. Acarreta, J.R.; De Haan, J.F.; Stammes, P. Cloud pressure retrieval using the O-2-O-2 absorption band at 477 nm. *J. Geophys. Res. Atmos.* **2004**, *109*. [CrossRef]
54. Williams, J.E.; Boersma, K.F.; Le Sager, P.; Verstraeten, W.W. The high-resolution version of tm5-mp for optimized satellite retrievals: Description and validation. *Geosci. Model Dev.* **2017**, *10*, 721–750. [CrossRef]
55. Kleipool, Q.L.; Dobber, M.R.; de Haan, J.F.; Levelt, P.F. Earth surface reflectance climatology from 3 years of omi data. *J. Geophys Res. Atmos.* **2008**, *113*. [CrossRef]